Journal of Applied Physics

Lattice stability and point defect energetics of $TiSi_2$ and $TiGe_2$ allotropes from first-principles calculations

Cite as: J. Appl. Phys. **129**, 085104 (2021); https://doi.org/10.1063/5.0029990
Submitted: 17 September 2020 . Accepted: 24 January 2021 . Published Online: 24 February 2021

David L. Brown, Kevin S. Jones, and Simon R. Phillpot

Journal of Applied Physics ARTICLE scitation.org/journal/jap

Lattice stability and point defect energetics of $TiSi_2$ and $TiGe_2$ allotropes from first-principles calculations

Cite as: J. Appl. Phys. **129**, 085104 (2021); doi: 10.1063/5.0029990
Submitted: 17 September 2020 · Accepted: 24 January 2021 ·
Published Online: 24 February 2021

David L. Brown, Kevin S. Jones, and Simon R. Phillpot[a)]

AFFILIATIONS

Department of Materials Science and Engineering, University of Florida, Gainesville, Florida 32611, USA

[a)]**Author to whom correspondence should be addressed:** sphil@mse.ufl.edu

ABSTRACT

This work determines the phase stabilities and point defect energetics of $TiSi_2$ and $TiGe_2$ allotropes using density functional theory. The primary focus is on the C49 and C54 allotropes, which compete during $TiSi_2$ phase formation. It is found that the ground state structure for $TiGe_2$ is the C54 allotrope, desirable for its low sheet resistance, while the less desirable, higher resistance C49 allotrope forms the ground state structure of $TiSi_2$. A first attempt to understand the Ge atom's role in lowering the enthalpy of formation for the C54 structure is made from the perspective of the extended Born model. Charge density differences, the density of states, and Bader charge analysis show that these systems are predominantly ionically bonded, with the Ge atoms introducing additional covalent bond stability for the C54 allotrope. It is known that higher temperatures favor C54 formation in $TiSi_2$. Helmholtz free energy calculations for $TiSi_2$ suggest that the vibrational free energy does not drive the system to the C54 phase. The formation energies of certain point defects within the C49 structure of $TiSi_2$ are less than 1 eV, which is consistent with experiments that show high defect concentrations. Thus, the driving force for C54 formation at higher temperatures may be related to the high defect concentration in the C49 allotrope.

INTRODUCTION

The relentless decrease in the feature size of microelectronic devices means that there is a need to constantly reduce contact resistance between the semiconductor and the metal interconnects in order to realize the desired increases in device performance. Silicides such as tungsten disilicide (WSi_2), titanium disilicide ($TiSi_2$), nickel disilicide ($NiSi_2$), and cobalt disilicide ($CoSi_2$) have long been used to reduce the contact resistance. These silicides interface between the semiconductor (usually Si) and the contact metal as an additional layer and reduce contact resistance by lowering the Schottky barrier height between the metal and semiconductor. Among the silicides, $TiSi_2$ is the ubiquitous low contact resistance silicide used for Complementary Metal–Oxide–Semiconductor (CMOS) devices because of its low thermal budget and excellent oxidation resistance.[1,2] Additionally, it has the benefit of low defect concentration in the contact region with silicon. Two allotropes of $TiSi_2$ are of particular interest: the lower contact resistance C54 structure and the higher contact resistance C49 structure.[1–4] The C49 phase forms at lower temperatures (around 600 °C) and transforms into C54 at temperatures above 700 °C. This transformation has been the focus of much analysis.[3,4] The C49 allotrope is observed at a lower temperature but is considered to be a metastable precursor phase to C54. Several different origins for this phase sequence have been proposed. One argument states that the interfacial energies for $TiSi_2$/amorphous–TiSi and $TiSi_2$/Si interface are lower for the C49 structure than for the C54 structure. As a result, the C49 structure forms first.[5,6] Another argument is made based on the majority atom experiencing twice the vacancy diffusion of the minority atom.[3,7,8] In the case of the silicide, the Si atoms have greater mobility, and Si is known to be the dominant diffuser in $TiSi_2$.[7,9] However, the mechanism by which this greater Si mobility causes C49 to be formed first remains unclear.[3,7,10]

In addition to exploring why C49 is the precursor, several experiments have manipulated the environment of the C49–C54 solid reaction to understand the transformation from one to the other. This includes introducing n-type and p-type dopants that tend to suppress the C49–C54 phase transformation, presumably

by increasing the vacancy diffusion energy barrier.[11] Experiments have also investigated the role of the Ti deposition dimensions and found that a decrease of Ti dimensions correlates with an increase of the C49–C54 transformation energy barrier.[5,12] This phenomenon has been called the "fine line effect," relating to the reduction of nucleation sites for C54.[13–15] From TEM micrographs, C54 has been observed to grow from the triple-point grain boundaries of C49, the concentration of which decreases along with the Ti thickness.[16,17] Since device scaling requires thinner films, the very thin films will exacerbate the trend, making it even harder to form the C54 phase. It is thus desirable to understand the mechanisms that control the C54 formation temperature.

The addition of a third element has been shown to lower the temperature required for the formation of the C54 structure. Previous works have reported using Ta or Mo to form a ternary solid-state reaction to reduce the C54 formation temperature.[1,10] It has also been observed that the introduction of Ge reduces the C54 formation temperature when forming silicide on a $Si_{1-x}Ge_x$ layer. This layer is grown as a co-flow process requiring only a single step.[18–21]

The introduction of $Si_{1-x}Ge_x$ films at the source–drain regions introduces compressive strain in microdevices, thereby improving the hole mobility in the channel.[22] The $Si_{1-x}Ge_x$ films produce C49 and C54 allotropes of $Ti(Si_{1-x}Ge_x)_2$.[18,19] Initially, it appears that the Ti-$Si_{1-x}Ge_x$ solid reaction solves the prior problems, as the $Si_{1-x}Ge_x$ film provides the benefit of enhancing hole mobility and reducing the C49–C54 transformation temperature. Although Ge may reduce the C54 formation temperature, Ge segregation introduces another problem for thinner films of Ti: the bilayer reaction still requires higher temperatures (≥125 °C) for complete C54 transformation with reduced Ti thickness.[5] Specifically, with increased temperature, the Ge segregation into the grain boundaries increases, forming a region of $Si_{1-y}Ge_y$ (a different concentration from the $Si_{1-x}Ge_x$ film) extending from the surface to the substrate. The pillars of $Si_{1-y}Ge_y$ increase the sheet resistance beyond tolerance.[5] Aldrich *et al.* also found that the C49–C54 transformation energy barrier still increased for thinner Ti layers (less than 10 nm thick). Therefore, the "fine line effect" still plays a key role, and higher temperatures are needed for C54 formation. An additional problem is that Ge segregation worsens with increased temperature.[5] Because $Si_{1-x}Ge_x$ alloys will continue to be employed to introduce compressive strain, understanding of the $Ti(Si_{1-x}Ge_x)_2$ allotropes is beneficial for semiconductor processing.[20,23]

Like $TiSi_2$, the $TiGe_2$ phase forms as C49 and C54 allotropes. However, in this case, C49 is not observed as a precursor phase to C54. The solid-phase reaction of Ti–Ge forms the precursor phase Ti_6Ge_5, with the C54 structure forming during the continued reaction of Ge with Ti_6Ge_5 through a nucleation process.[19,24] While not part of the normal evolution of the silicide, metastable C49 has been synthesized using co-evaporation of $Ti_{0.33}Ge_{0.67}$ followed by crystallization to C49 at 315 °C.[25] The metastability of the $TiGe_2$ C49 allotrope suggests that Ge plays a role in reducing favorability for C49, thereby reducing the C49–C54 transformation barrier.

There exists a third allotrope of interest in the $TiSi_2$ system, the C40 structure.[26] It has a lower electrical resistance than C49 and transforms into C54 with subsequent annealing.[17,26,27] Due to lattice mismatching, C49 cannot form during the transformation from C40 to C54, so the high resistance of the C49 structure is bypassed. The C40 structure has been synthesized with laser pulse annealing and characterized with Raman spectroscopy and transmission electron microscopy.[17,26–28] The formation of low resistance C54 might be achieved without the presence of C49, if one can form the C40 phase.

This work will develop a theoretical understanding of the $TiGe_2$ phase, with the objective of more fully understanding why the Ti-$Si_{1-x}Ge_x$ bilayer reactions reduce the C54 formation temperature. Also, the lattice stability and defects in $TiSi_2$ and $TiGe_2$ will be characterized and expanded to include the C40 phase. A thermodynamic perspective of these solid-state reactions will be presented based on evidence from Density Functional Theory (DFT) calculations with the goal of better understanding the driving forces associated with these critical phase transformations.

$TISI_2$ AND $TIGE_2$ STRUCTURE

Figure 1 illustrates the structures of the silicide and germanide allotropes. C49 has a base-centered orthorhombic (Fddd) structure. C54 has a face-centered orthorhombic (Cmcm) structure. C40 has a hexagonal type ($P6_222$) structure. The most noticeable structural difference between the three is in the periodic layering of Si/Ge. The C49 structure has two distinct bonding environments for the Si/Ge atoms. As Fig. 1(c) shows, there is a Si/Ge monolayer with fourfold bonding in the plane. There is also a Ti–Si/Ge layer, in which the Si/Ge is covalently bonded with two nearest neighbors. The monolayer will be denoted as 4-NN for its four nearest Si/Ge neighbors, while the Ti–Si/Ge layer will be denoted as 2-NN for its two nearest Si/Ge. The other allotropes have higher symmetry than C49. Figure 1(a) is the ab perspective of the C40 allotrope in which the hexagonal structure is evident. Figure 1(b) from the bc perspective of C40 shows that the Si atoms have two nearest neighbor atoms and a periodic stacking. Figure 1(d) shows that the Si atoms in C54 also have two nearest neighbors.

CALCULATION METHODS

The Vienna *Ab initio* Simulation Package (VASP) is used for the electronic-structure calculations at the level of Density Functional Theory (DFT). The Generalized Gradient Method (GGA) and the Strongly Constrained and Appropriately Normed (SCAN) functional are used for the exchange-correlation in this work; SCAN is a new meta-GGA functional, which has proven to be well-suited for characterizing transition metal reactivity.[29–37] The [3d 4s 4p] orbitals are included for the calculations with Ge potentials,[38] while the [3d 4p 4s] orbitals are included for the calculations with Ti potentials. The Si potential includes [2s 2p] orbitals.

The plane wave cutoff used for relaxation is 520 eV, and the Monkhorst–Pack mesh method is used for Brillouin zone sampling.[39] The C49 structure is relaxed with a $10 \times 3 \times 10$ k-point mesh, the C54 structure with a $7 \times 4 \times 4$ mesh, and the C40 structure with a $9 \times 9 \times 5$ mesh. The unit cell dimensions for each calculation are presented in Table I. These large k-point meshes are needed because of the small unit cell sizes, which are of different dimensions for each system. The supercell dimensions and ion positions are relaxed simultaneously until the force on each atom is less than 0.01 eV/Å, with components of stress less than 0.02 GPa. The space groups of the calculated structures are determined using

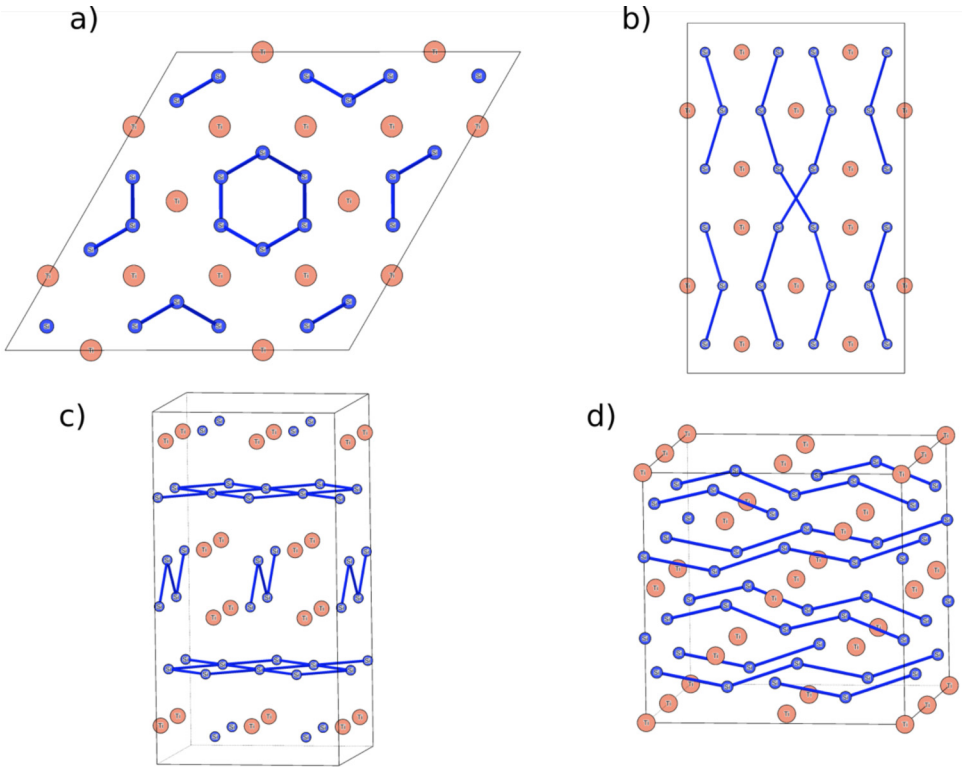

FIG. 1. The hexagonal C40 structure from the (a) ab and (b) bc perspectives. The base-centered orthorhombic for C49 (c) showing two structurally different layers; the C54 (d) face-centered orthorhombic structure; the silicon atoms represented as small circles (dark blue) and the titanium atoms are large circles (light orange).

TABLE I. Structure and formation enthalpies of $TiSi_2$ and $TiGe_2$ structures, with a comparison to prior results.

Phase	Space group		a (Å)	b (Å)	c (Å)	Enthalpy (meV/atom)
$TiSi_2$						
C40	$P6_222$	PBE-GGA	4.727	4.727	6.598	−535
		SCAN	4.707	4.70	6.543	−491
		FLAPW-GGA[53]	4.731	4.731	6.570	−497
C49	Cmcm	PBE-GGA	3.548	13.568	3.578	−557
		SCAN	3.524	13.510	3.553	−523
		FLAPW-GGA[53]	3.541	13.617	3.576	−523
		PBE-GGA[38]	3.559	13.498	3.572	−562
C54	Fddd	PBE-GGA	4.795	8.254	8.583	−550
		SCAN	4.786	8.230	8.490	−518
		FLAPW-GGA[53]	4.806	8.268	8.560	−516
		PBE-GGA[38]	4.809	8.260	8.567	−556
$TiGe_2$						
C40	$P6_222$	PBE-GGA	4.959	4.959	6.822	−422
		SCAN	4.892	4.892	6.755	−444
C49	Cmcm	PBE-GGA	3.689	14.320	3.714	−422
		SCAN	3.643	14.088	3.675	−452
C54	Fddd	PBE-GGA	5.073	8.663	8.827	−433
		SCAN	5.021	8.525	8.716	−460
		PBE-GGA[38]	5.083	8.677	8.826	−414

TABLE II. The stoichiometric ($\mu_{Si} = \mu_{Si}^{mid}$ and $\mu_{Ti} = \mu_{Ti}^{mid}$), Ti-rich ($\mu_{Si} = \mu_{Si}^{min}$ and $\mu_{Ti} = \mu_{Ti}^{bulk}$), and Si-rich ($\mu_{Si} = \mu_{Si}^{bulk}$ and $\mu_{Ti} = \mu_{Ti}^{min}$) concentration limit defect energies for $TiSi_2$. The calculations are performed with PBE-GGA; units are eV.

	V_{Si}	V_{Ti}	Si_{Ti}	Ti_{Si}
C49				
Ti-rich	2-NN: −0.003	2.73	5.18	2-NN: −0.567
	4-NN: 0.212			4-NN: 0.119
Stoichiometric	2-NN: 0.418	1.89	3.92	2-NN: 0.695
	4-NN: 0.633			4-NN: 1.38
Si-rich	2-NN: 0.839	1.04	2.65	2-NN: 1.96
	4-NN: 1.05			4-NN: 2.64
C54				
Ti-rich	1.67	3.87	5.09	0.089
Stoichiometric	2.08	3.04	3.85	1.33
Si-rich	2.49	2.22	2.61	2.56

the FINDSYM package.[40] The density of states and formation energies are calculated with the tetrahedron method[41] and a Methfessel–Paxton pre-convergence.[42] For the point defect calculations, the C54, C40, and C49 structures are relaxed using supercells of $3 \times 2 \times 2$, $3 \times 3 \times 2$, and $5 \times 1 \times 5$ unit cells, respectively. These dimensions are chosen to yield approximately cubic supercells. The sampling scheme for defect calculations is a $3 \times 3 \times 3$ k-point sampling mesh. The energy differences between the unit cell calculations with large k-point values and the supercell calculations with smaller k-point values are less than 5 meV. This energy difference has only a small effect on the point defect calculations presented in Table II.

The supercell dimensions are fixed for point defect calculations. While there are still defect to defect interactions between supercells, the use of a fixed volume condition attempts to represent the conditions of an isolated defect.[43] $TiSi_2$ and $TiGe_2$ are conductors, so charged defects are not considered for this work. The defect formation energies are calculated using the standard equations,

$$\text{Vacancy:} \quad \Delta H_f = E_{defect}[V_{Si\,or\,Ti}] - E_{perfect} - \mu_{Si\,or\,Ti}, \tag{1}$$

$$\text{Frenkel:} \quad \Delta H_f = E_{defect}[V_{Si\,or\,Ti}] + E_{defect}[Si_i\ \text{or}\ Ti_i] - 2E_{perfect}, \tag{2}$$

$$\text{Substitution:} \quad \Delta H_f = E_{defect}[Si/Ti_{Si\,or\,Ti}] - E_{perfect} + \mu_{Si\,or\,Ti} - \mu_{Ti\,or\,Si}. \tag{3}$$

The chemical potentials μ_{Si}, μ_{Ge}, and μ_{Ti} in Eqs. (1)–(3) reflect the reservoirs for atoms added and removed during the formation of the defect. These chemical potentials are taken as the energies per atom of the pure bulk elements, as calculated with DFT. However, chemical potentials taken from the respective bulk elemental forms ($\mu_{Si} = \mu_{Si}^{bulk}$, $\mu_{Ge} = \mu_{Ge}^{bulk}$, and $\mu_{Ti} = \mu_{Ti}^{bulk}$) do not consider the sensitivity to concentration conditions under which the crystal is grown.

As a function of concentration, the chemical potential of the atoms must satisfy restrictions such that $\mu_{Si} \leq \mu_{Si}^{bulk}$, $\mu_{Ge} \leq \mu_{Ge}^{bulk}$, and $\mu_{Ti} \leq \mu_{Ti}^{bulk}$, with the variables μ_{Si}^{bulk}, μ_{Ge}^{bulk}, and μ_{Ti}^{bulk} calculated from the elemental bulk energy per atom. If these conditions are not satisfied, the $TiSi_2$ or $TiGe_2$ phases will decompose into pure bulk Si, Ge, and Ti. A second constraint comes from constituent atoms being in equilibrium with $TiSi_2$ and $TiGe_2$. μ_{Si}, μ_{Ge}, and μ_{Ti} are equal to the chemical potentials per each pair of $TiSi_2$ and $TiGe_2$ pure bulk phases such that $\mu_{TiSi_2}^{bulk} = \mu_{Ti} + 2\mu_{Si}$ and $\mu_{TiGe_2}^{bulk} = \mu_{Ti} + 2\mu_{Ge}$.Therefore, the concentration extremes that can be tested are the Si/Ge-rich ($\mu_{Si} = \mu_{Si}^{bulk}$ and $\mu_{Ge} = \mu_{Ge}^{bulk}$) or Ti-rich ($\mu_{Ti} = \mu_{Ti}^{bulk}$) conditions. From these restrictions, the chemical potential at Si/Ge-rich and Ti-rich conditions are given as Eqs. (4) and (5), respectively,

$$\mu_{Ti}^{min} = \mu_{TiSi_2\,or\,TiGe_2}^{bulk} - 2\mu_{Si\,or\,Ge}^{bulk}, \tag{4}$$

$$\mu_{Si}^{min} = \frac{1}{2}(\mu_{TiSi_2\,or\,TiGe_2}^{bulk} - \mu_{Ti}^{bulk}). \tag{5}$$

These chemical potentials are combined with Eqs. (1)–(3) to determine defect formation energies; a third growth condition is stoichiometric, which represents the concentration midpoint. To be explicit, the Si/Ge-rich region is defined as $\mu_{Si} = \mu_{Si}^{bulk}$ and $\mu_{Ge} = \mu_{Ge}^{bulk}$ with $\mu_{Ti} = \mu_{Ti}^{min}$; the Ti-rich region is defined as $\mu_{Ti} = \mu_{Ti}^{bulk}$ with $\mu_{Si} = \mu_{Si}^{min}$ and $\mu_{Ge} = \mu_{Ge}^{min}$. Previous works have shown the relationship between concentration and potential energy to be linear.[44] Therefore, the stoichiometric chemical potential is taken as the linear midpoint between these two conditions: $\mu_{Ti}^{mid} = \frac{1}{2}(\mu_{Ti}^{bulk} + \mu_{Ti}^{min})$ and $\mu_{Si}^{mid} = \frac{1}{2}(\mu_{Si}^{bulk} + \mu_{Si}^{min})$ and $\mu_{Ge}^{mid} = \frac{1}{2}(\mu_{Ge}^{bulk} + \mu_{Ge}^{min})$ (Table III).

With regard to the distribution of charge in the system, isosurfaces of the charge density difference (CDD) are plotted around the atoms first coordination shell so that the charge transfer can be visualized. The CDD, $\Delta\rho_{diff}(r)$, is defined as the difference between the charge density of the ordered phase, $\rho_{phase}(r)$, and the sum of the charge densities of the single element, $\rho_\alpha(r - r_\alpha)$ when the other elements are removed from the supercell: $\Delta\rho_{diff}(r) = \rho_{phase}(r) - \sum_\alpha \rho_\alpha(r - r_\alpha)$. This definition thus represents the charge redistribution when atoms are brought together to form the phase.[45,46]

TABLE III. The stoichiometric ($\mu_{Ge} = \mu_{Ge}^{mid}$ and $\mu_{Ti} = \mu_{Ti}^{mid}$), Ti-rich ($\mu_{Ge} = \mu_{Ge}^{min}$ and $\mu_{Ti} = \mu_{Ti}^{bulk}$), and Ge-rich ($\mu_{Ge} = \mu_{Ge}^{bulk}$ and $\mu_{Ti} = \mu_{Ti}^{min}$) limit defect energies for $TiGe_2$. The calculations are performed with PBE-GGA; units are eV.

	V_{Ge}	V_{Ti}	Ge_{Ti}	Ti_{Ge}
C49				
Ti-rich	2-NN:−0.118	1.81	4.05	2-NN:−0.398
	4-NN:−0.698			4-NN:−0.709
Stoichiometric	2-NN:0.199	1.17	3.10	2-NN:0.553
	4-NN:−0.381			4-NN:0.242
Ge-rich	2-NN:0.516	0.541	2.14	2-NN:1.50
	4-NN:−0.0638			4-NN:1.19
C54				
Ti-rich	0.892	2.96	4.39	−0.277
Stoichiometric	1.22	2.31	3.42	0.698
Ge-rich	1.54	1.66	2.45	1.67

A semi-quantitative study of the ionic bonding component and defect charge transfer is performed with the Bader analysis code from the Henkelman group.[47–50] The importance of charge transfer for the enthalpy of the formation of phases and defects was shown in Liu *et al.*[51] based on the extended Born model. This model considers partial polarization in a material. Like Liu *et al.*, this work will study the C49 and C54 allotropes from the extended Born model perspective, since that model takes into account covalent bonds and partial charge transfer,[52]

$$\Delta H_f = \Delta H_{\text{at}} + (\Delta U_i - \Delta U_{\text{ea}}) + \Delta H_{\text{el}} + \Delta H_{\text{cov}}. \quad (6)$$

The enthalpy of formation in Table I is represented as ΔH_f in the extended Born model. ΔH_{at} represents the covalent energy between atoms of the same element, taking into account that there is no charge transfer between like atoms. The electron affinity and ionization energy for the isolated atoms are represented by the second term $(\Delta U_i - \Delta U_{\text{ea}})$. ΔH_{el} is the electrostatic lattice energy for localized bonding, and ΔH_{cov} corresponds to the heat of formation of the covalent lattice of the crystal, which depends on valence electron orbitals and coordination.

There are multiple steps to evaluating Eq. (6). In the first step, the binary alloy is separated such that its energy can be referenced to its pure components: this is the way that ΔH_f is calculated. In the second step, the atoms of the pure phases are disassociated into isolated atoms such that $\Delta H_t = \frac{E_{\text{tot}}}{N} - \sum_i E_i(r \to \infty)$. In the third step, these isolated atoms are ionized, enabling an estimate of the partial charge transfer. In the fourth step, the electrostatic attraction within the crystal is determined as $\Delta H_{\text{el}} = \frac{N_A \alpha q_i q_j e^2}{4\pi\epsilon_0 r_0}\left(1 - \frac{1}{n}\right)$, where N_A is Avogadro's constant, α is the Madelung constant for the specific crystal lattice, q_i and q_j are the partial charges of the anion and cation, e is the charge of the electron, r_0 is the interatomic distance between the cation and anion, and n is an empirical quantity for the distance dependence of repulsion. In the last step, the total effect is determined by subtraction. Though the partial charge is not quantitatively defined in DFT, the extended Born model does allow the relative importance of ionic and covalent bond mixing of the lattice enthalpy to be semi-quantitatively determined.

The extended Born model will be applied to these phases through the qualitative insight of quantitative calculations gained from the density of states (DOS), Bader analysis, and CDD. DOS yields insight into the covalent bond strength through the phase's pseudogap, while Bader analysis qualitatively describes the importance of partial charge transfer. The conclusions provided from both techniques should be consistent with CDD.

PHASE STABILITY

The enthalpic calculations for the $TiSi_2$ C40, C49, and C54 allotropes are shown in Table I. For $TiSi_2$, the C49 system is the most stable structure. The calculations with the GGA functional predict that its enthalpy is 7 meV/atom lower than that of C54; the SCAN functional predicts it to be 5 meV/atom lower. The C49 structure is even more stable with respect to the C40 structure: by 22 meV/atom (GGA) and 32 meV per atom (SCAN). These results agree with those of Jain *et al.* [38] However, they do not agree with the results of Colinet *et al.*,[53] which predict a difference of 34 meV/ atom for $TiSi_2$ C49 and 34 meV/atom for $TiSi_2$ C54. Both Colinet *et al.* and Jain *et al.* used PBE-GGA functional for calculations. However, Colinet *et al.* performed structure relaxations with PBE-GGA, then calculated formation energies using FLAPW-GGA. The use of different functionals in the calculations explains these differences.

The enthalpies of the formation for the $TiGe_2$ C49 and C40 allotropes have not been calculated in previous works. As a baseline, we have calculated the enthalpy of formation for the $TiGe_2$ C54 allotrope to compare with an earlier high throughput work.[54] In Table I, the lowest energy allotrope of $TiGe_2$ is C54, with the enthalpies of the C49 and C40 structures both being 11 meV/atom higher for the PBE-GGA functional. The SCAN functional also predicts that the C54 structure is the most stable, with the C40 structure being 8 meV/atom higher and the C49 structure a further 8 meV/atom higher.

Sun *et al.* mined data from the materials project and evaluated the influence of the chemistry and composition for various polymorphic compounds.[55] The upper limit of the convex hull for metastability was found to be 70 meV for most inorganic materials. That is, structures with enthalpies of formation above the convex hull by less than 70 meV have a significant chance of being metastable and, thus, may be manifested experimentally. Applying that criterion to this system, the $TiGe_2$ C49 and TiSi2 C40 allotropes are known metastable structures and indeed within the 70 meV stability upper limit. On this basis, the $TiGe_2$ C40 structure may be metastable also.

The relative lattice stability between the allotropes might change at higher temperatures, so the vibrational free energy is calculated using the Phonopy package with the PBE-GGA functional.[56] Due to the presence of metal atoms, the Methfessel–Paxton method is utilized to determine the forces between the atoms. The vibrational free energy calculated is a function of temperature in the harmonic approximation, which assumes that the thermal expansion does not significantly affect lattice phonons. The Helmholtz free energy is expressed as

$$A(T) = E_{\text{latt}} + F_v(T),$$

when E_{latt} is the lattice's total internal energy and $F_v(T)$ is the vibrational contribution of the free energy.[57]

At $T = 0$ K, the zero-point energy contributions for $TiSi_2$ C40, C49, and C54 are 14.74 kJ mol^{-1}, 14.26 kJ mol^{-1}, 13.6 kJ mol^{-1}, respectively. The calculated values of Colinet *et al.*[53] are 14.2 kJ mol^{-1}, 15.2 kJ mol^{-1}, and 14.5 kJ mol^{-1}. This work shows closer agreement for the C40 allotrope, but a disagreement emerges for C49 and C54 in terms of value and order. The $TiGe_2$ allotropes zero-point energies are 9.75 kJ mol^{-1}, 9.36 kJ mol^{-1}, and 5.94 kJ mol^{-1}, respectively. These values follow the same order as in $TiSi_2$ but are about one-half lower, which corresponds with mass differences being nearly a half between Ge and Si.

Figure 2 represents the Helmholtz free energy for the $TiSi_2$ and $TiGe_2$ allotropes. In Fig. 2(a), the Helmholtz free energy is −639 kJ mol^{-1}, −640 kJ mol^{-1}, and −641 kJ mol^{-1} for C40, C49, and C54, respectively, at $T = 0$ K keeping to the same order as enthalpy of formation in Table I. With increasing temperature, the vibrational

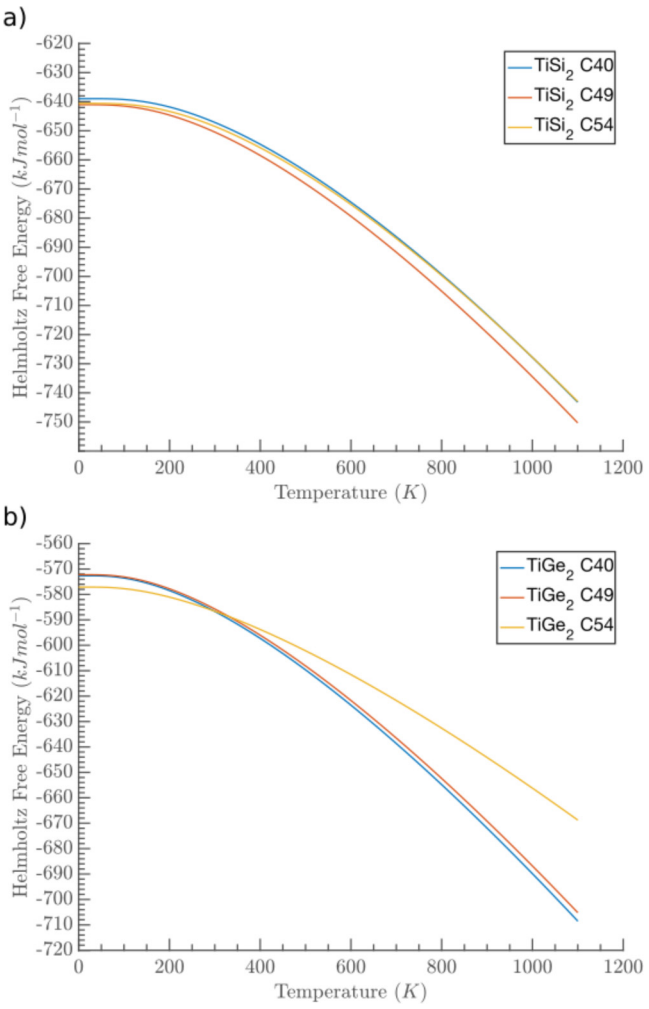

FIG. 2. The Helmholtz free energy for the $TiSi_2$ (a) and $TiGe_2$ (b) allotropes.

free energy difference between C49 and C54 increases, while the difference between the C54 and C40 decreases. The C54 and C40 allotrope free energies cross at $T = 980$ K with the C40 free energy being lower at higher temperatures. There is considerable uncertainty in the transition temperature because the free energies cross at a very shallow angle and because these harmonic approximation calculations do not take thermal expansion into account. The C54 and C49 free energies continue to diverge with C49 having the lowest free energy. Colinet *et al.* predicts a free energy crossing from C49 to C54 at T = 1100 K, which suggests that the vibrational free energy contributes to C54 being the more stable structure at higher temperatures.[53] However, this work does not show a crossing from C49 to C54; thus, the vibrational free energy is not shown to be a contributor for the $TiSi_2$ C54 allotrope forming at higher temperatures. Additionally, the vibrational free energy contribution reduces the Helmholtz free energy of the C40 allotrope below C54 at T = 980 K. These differences could simply arise from the use of the LAPW functionals used in Colinet *et al.*, or our use of the Methfessel–Paxton scheme.

Figure 2(b) shows the Helmholtz free energy for the $TiGe_2$ phase. The figure suggests that $TiGe_2$ C54 is stable over a wide range of temperatures, with it being the most stable or metastable up to room temperature; the fee energies of the C49 and C40 allotropes cross near room temperature. Although there is still uncertainty in this transition temperature, it is less than for the case of $TiSi_2$ because the free energies cross at a much greater angle and because at these relatively low temperatures the effects of thermal expansion are considerably small. As mentioned earlier, the C40 structure has never been experimentally observed, and the C49 structure is only observed with non-equilibrium growth methods. However, the Helmholtz free energy suggests the free vibrational energy drives the C40 and C49 allotropes into the most stable structures beyond room temperature. Thus, the vibrational free energy is not a contributor to C54 being the most stable phase at processing temperatures (600 °C–700°).

DEFECT ENERGETICS AND CHARGE

The concentrations of point defects, such as antisites and vacancies, impact the lattice stability and phase equilibria of intermetallic alloys.[46] Therefore, it is necessary to determine the formation energy of defects in $TiSi_2$ and $TiGe_2$. The point defects energies of these systems are compiled in Table II. Because of the inequivalence of the Si/Ge atom lattice sites in the C49 structure, the vacancy formation energies for the 2-NN and 4-NN sites are calculated separately.

The defect formation energies may change due to the chemical potential's sensitivity to the reactants' concentrations during the crystal growth. Thus, calculating the chemical potential at different concentrations is necessary to this work. In the following tables, the three different sets of values for chemical potential described above are used to calculate the defect energetics; the three growth conditions are (i) Ti-rich ($\mu_{\mathrm{Si\ or\ Ge}} = \mu^{\mathrm{min}}_{\mathrm{Si\ or\ Ge}}$ and $\mu_{\mathrm{Ti}} = \mu^{\mathrm{bulk}}_{\mathrm{Ti}}$), (ii) Si/Ge-rich ($\mu_{\mathrm{Si\ or\ Ge}} = \mu^{\mathrm{bulk}}_{\mathrm{Si\ or\ Ge}}$ and $\mu_{\mathrm{Ti}} = \mu^{\mathrm{min}}_{\mathrm{Ti}}$), and (iii) stoichiometric ($\mu_{\mathrm{Si\ or\ Ge}} = \mu^{\mathrm{mid}}_{\mathrm{Si\ or\ Ge}}$ and $\mu_{\mathrm{Ti}} = \mu^{\mathrm{mid}}_{\mathrm{Ti}}$). Due to the thermodynamic equilibrium restriction ($\mu^{\mathrm{bulk}}_{\mathrm{TiSi_2}} = \mu_{\mathrm{Ti}} + 2\mu_{\mathrm{Si}}$ and $\mu^{\mathrm{bulk}}_{\mathrm{TiGe_2}} = \mu_{\mathrm{Ti}} + 2\mu_{\mathrm{Ge}}$), the chemical potentials cannot simultaneously be equal to their bulk values. This restriction is a linear equation; thus, the line is described with only the end points, and the stoichiometric concentration is taken as the midpoint of the line.

For the C49 structure of $TiSi_2$, the lowest defect formation energy by far (−0.567 eV) is the Ti-rich environment for the Ti_{Si} on the 2-NN site (i.e., within the TiSi layer); the corresponding value for the 4-NN site is 0.119 eV. The stoichiometric condition shows an increase of defect formation energy with 2-NN still below 1 eV and 4-NN now above 1 eV. In the Si-rich case, the formation energies increase to well above 1 eV for both the 2-NN (1.96 eV) and 4-NN (2.64 eV). In all but the Ti-rich case, the lowest energy defect is the V_{Si} defect; stoichiometric concentrations show both 2-NN (0.418 eV) and 4-NN (0.633 eV) sites are below 1 eV; the Si-rich case shows 2-NN (0.839 eV) below 1 eV, while 4-NN (1.05 eV) is slightly above 1 eV. Overall, the data suggest a disfavor

for defects that remove Ti; in particular, the V_{Si} and Ti_{Si} defects in the Ti-rich case have negative formation energies, suggesting C49 has a much stronger driving force to becoming sub-stoichiometric in Si than does C54.

The lowest formation energy for the C54 allotrope under Ti-rich conditions is the Ti_{Si} defect. This defect formation is only 0.089 eV; however, the formation energy increases above 1 eV for the stoichiometric case. Two major points can be deduced from the data for C54: defects that remove Ti are less favorable at Ti-rich conditions, and the higher defect energies suggest that C54 has lower defect concentrations than C49. The vacancy defect energies are higher than in C49, except for the Si-rich case of V_{Ti}. These vacancy defect energies can be compared to the work of Wang *et al.* Using DFT with the GGA functional, Wang *et al.* found $E(V_{Si}) = 2.39$ eV and $E(V_{Ti}) = 2.40$ eV in the C54 structure; this work found $E(V_{Si}) = 2.49$ eV and $E(V_{Ti}) = 2.22$ eV at the Si-rich limit. At the Ti-rich limit, their corresponding energies are $E(V_{Si}) = 1.53$ eV and $E(V_{Ti}) = 4.07$ eV, while this work found $E(V_{Si}) = 1.67$ eV and $E(V_{Ti}) = 3.87$ eV.[58] These defect formation energy data is consistent with the data presented here. The slight differences can be attributed to our calculations using a larger basis set for the Ti than that of Wang *et al.*; the presumption is that the larger basis set will result in more reliable values for defect energies. Miglio *et al.* calculated defect formation energies for C49 with molecular dynamics simulations using a semiempirical tight-binding interatomic potential.[59] They calculated the vacancy formation energies of Si to be 0.09 eV and 0.89 eV for 2-NN and 4-NN, respectively. They determined the vacancy formation energy of Si in the C54 structure to be 1.41 eV.[59] The differences with the values from DFT methods are not concerning since DFT is known to generally provide higher materials fidelity than tight-binding methods.

The defect energies for $TiGe_2$ C49 have similarities to the $TiSi_2$ C49 phase. Both have low defect formation energies for $V_{Si/Ge}$ and $Ti_{Si/Ge}$. Both V_{Ge} and Ti_{Ge} show negative formation energies in the Ti-rich case, and the V_{Ge} defect shows negative energies in all cases except the 2-NN sites. This data suggest that $TiGe_2$ C49 may not be observed with equilibrium growth methods because of these spontaneous defect formations. Another difference is the formation energies for the $TiGe_2$ 4-NN defects are lower than for the 2-NN defects, which is the opposite for $TiSi_2$. The only negative formation energy for $TiGe_2$ C54 is V_{Ge} (−0.277 eV) in Ti-rich conditions. However, $TiGe_2$ C54 has mostly non-negative defect formation energies, unlike C49, which coincides with C54 being observable under equilibrium growth methods. In general, C49 formation energies are lower than $TiSi_2$ allotropes, so $TiGe_2$ can be expected to have higher defect concentrations than $TiSi_2$ C54.

For binary systems containing transition and non-transition metals, the point defect formation energies can be reduced with charge transfer between the anions and cations.[51] As discussed, the $TiGe_2$ and TSi_2 phases show a significant difference in formation energies for vacancies and substitution. Therefore, the effect of partial charge transfer on stabilizing the $TiSi_2$ and $TiGe_2$ defects is explored with Bader analysis.

Only the nearest neighbor atoms around the defect are considered, so charge balance between these atoms is not expected. However, convergence was checked by matching the number of electrons in the potential files with the Bader analysis total electron output. The charge transfer was calculated in the same manner as the pure phase. The calculated total electron charge of an isolated atom species in the supercell subtracted the nearest neighbor defect atom. The difference determines the amount of charge gained or lost for the Ti (cation) and Si (anion) nearest neighbor.

Bader analysis is a limited tool for defect charge transfer for two reasons. First, as has been mentioned, it is a semi-qualitative method. The second reason is related to the calculating the charge of a vacancy defect. The effective charge of a vacancy can be expressed as $q_v = (q_{atom} - q_{vac}) - \sum_j q_j^{NN}$. Here, Δq_j^{NN} is the charge difference of the nearest neighbors; these charges are listed in Tables IV and V; q_{atom} is the total charge of an isolated atom, which is trivial to determine; q_{vac} is the charge of the defect volume, which the atom once occupied. The problem is calculating q_{vac}. In order for Bader analysis to calculate atom charge, the algorithm generates a Bader volume, which represent the approximate volume that an atom occupies then sums the total charge inside that volume. The Bader analysis algorithm does not determine a Bader volume for a vacancy defect and thus no charge inside a volume is summed to calculate q_{vac}. With these problems in mind, the magnitude of partial charge transfer at the nearest neighbors to the vacancy defect will be used for an indirect measure for the Coulomb potential.

Table IV shows the C49 $TiSi_2$ partial charge transfer of the nearest neighbor Si and Ti, with the defect energies for reference. Though the amount of charge transfer for the vacancy is unknown, it can be surmised that the region is electron depleted and thus positive. The antisite defect partial charges for both Ti_{Si} and Si_{Ti} cases are calculated by subtracting the isolated atom charge by the atom charge on the defect site. These antisite values are 0.83e for the Ti substitution and 0.14e for the Si substitution. A positive defect center suggests that the nearest neighbor Ti repels, while it provides electrostatic attraction with the nearest neighbor Si atoms.

TABLE IV. Charge transfer from Bader analysis of the nearest neighbor atoms of the vacancy and substitution defects in C49 $TiSi_2$.

Point defect	Formation energy (eV)	NN Si Δq	NN Ti Δq
V_{Si} 2-NN	Ti-rich: −0.003 Stoich.: 0.418 Si-rich: 0.633	−0.11e	0.38e
V_{Si} 4-NN	Ti-rich: 0.212 Stoich.: 0.633 Si-rich: 1.05	−0.45e	1.07e
V_{Ti}	Ti-rich: 2.73 Stoich.: 1.89 Si-rich: 1.04	−0.50e	1.05e
Ti_{Si} 2-NN	Ti-rich: −0.567 Stoich.: 0.695 Si-rich: 1.96	−0.57e	0.46e
Ti_{Si} 4-NN	Ti-rich: 0.119 Stoich.: 1.38 Si-rich: 2.64	−0.59e	0.9e
Si_{Ti}	Ti-rich: 5.18 Stoich.: 3.92 Si-rich: 2.65	−0.49e	1.1e

TABLE V. Charge transfer from Bader analysis of the nearest neighbor atoms of the vacancy and substitution defects in C54 $TiSi_2$.

Point defect	Formation energy (eV)	Si Δq	Ti Δq
V_{Si}	Ti-rich: 1.67	−0.51	0.80
	Stoich.: 2.08		
	Si-rich: 2.49		
V_{Ti}	Ti-rich: 3.87	−0.47	0.87
	Stoich.: 3.04		
	Si-rich: 2.22		
Ti_{Si}	Ti-rich: 0.089	−0.38	0.72
	Stoich.: 1.33		
	Si-rich: 2.56		
Si_{Ti}	Ti-rich: 5.09	−0.44	0.92
	Stoich.: 3.85		
	Si-rich: 2.61		

The charge of the Si atoms nearest to the defect, about −0.45e to −0.6e, are similar for all the defects, with the exception of V_{Si} 2-NN at −0.11e. The defects with formation energies below 1 eV show the smallest value for Ti charge: the V_{Si} 2-NN and Ti_{Si} 2-NN have nearest neighbor Ti charge values of 0.38e and 0.46e, respectively. However, the Ti_{Si} 4-NN defect is an exception with a partial charge of 0.9e. This defect shows a low formation energy below 1 eV for the Ti-rich case, but the energy increases to 2.64 eV for the Si-rich case. The partial charge transfer for Ti atoms near the Ti_{Si} 2-NN defect suggests the more positive partial charge contributes to the increase of formation energy. The Ti partial charge transfer for all defects above 1 eV is above 2.0e, which is consistent with a lower Ti charge relating to lower formation energy. An exception is the V_{Si} 4-NN site, but this defect has four nearest neighbor Si, which tend to stabilize the defect. The lowest defect formation energy is the Ti-rich Ti_{Si} defect, with a high Si nearest neighbor partial charge −0.57e and low Ti nearest neighbor partial charge of 0.46e. These results indicate that there is a relationship between the low defect formation energy and partial charge transfer for C49 $TiSi_2$.

Table V shows the C54 $TiSi_2$ partial charge transfer of nearest neighbor atoms. The partial charge defects are calculated in the same manner as C49; the Ti substitution yields a partial charge of 0.77e while Si is 0.04e. The nearest neighbor Si partial charge is similar for all of the defects. The defect with the lowest formation energy is Ti_{Si}, which relates to a high Ti substitution partial charge and a lower positive nearest neighbor Ti charge.

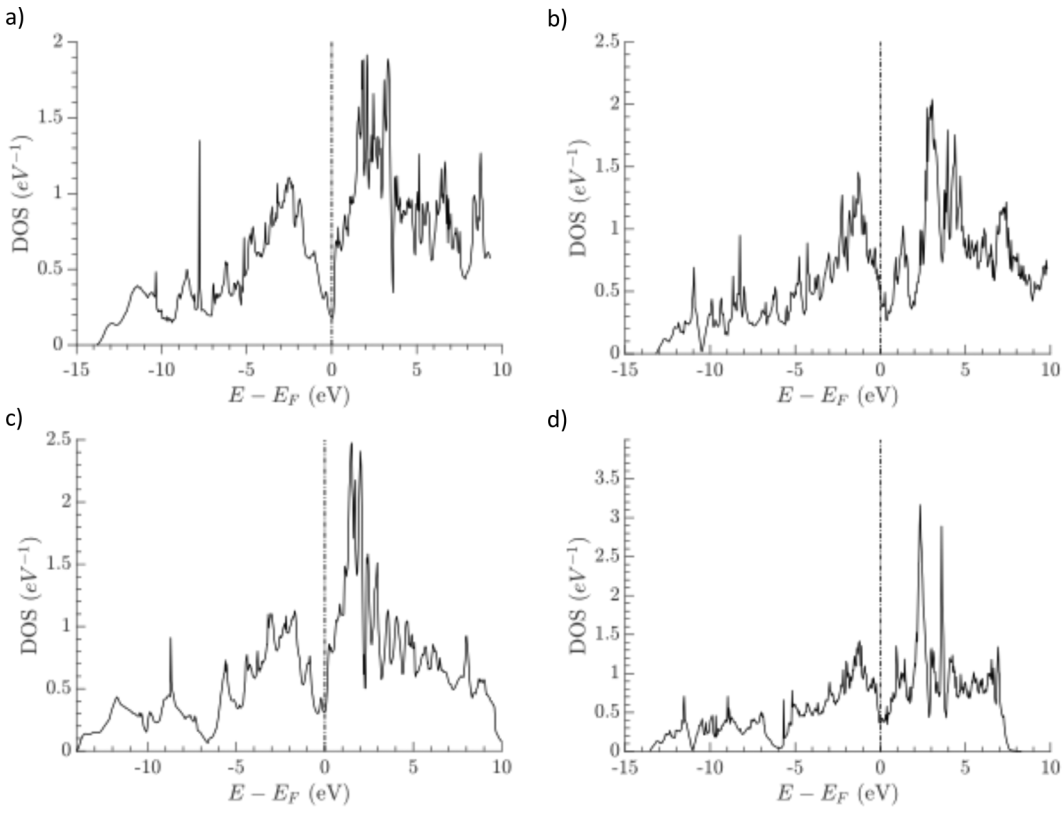

FIG. 3. The DOS for (a) C49 $TiSi_2$, (b) C54 $TiSi_2$, (c) C49 $TiGe_2$, and (d) C54 $TiGe_2$, calculated from SCAN functional and normalized by formula unit.

TABLE VI. Bader charges for $TiSi_2$ and $TiGe_2$.

Phase	Si	Ti
$TiSi_2$		
C49		+1.10e
2-N	−0.67e	
4-N	−0.43e	
C54	−0.57e	+1.14e
$TiGe_2$		
C49		+1.08e
2-N	−0.69e	
4-N	−0.39e	
C54	−0.57e	+1.14e

The nearest neighbor Si interatomic distance is less than that for Ti for all cases, so its Coulombic potential contribution is greater than Ti nearest neighbors. The substitution defects show a higher positive partial charge for Ti than Si, which corresponds with lower formation energy. Due to the defect centers being positive, the positive nearest neighbor Ti contributes repulsive electrostatics, which does not stabilize defects. Also, lower positive partial charges for nearest neighbor Ti correspond with the lower formation energies.

The partial charge transfer does affect the defect formation energies, but due to the limitations of Bader analysis, it is unclear how much the charge transfer reduces formation energy compared to lattice relaxation. If an algorithm that calculates vacancy charge is developed, a future work could include a more quantitative work, which could compare the contribution of lattice relaxation with partial charge transfer.

ELECTRONIC STRUCTURE AND BONDING

The Density of States (DOS) is calculated from the modern meta-GGA SCAN functional. Figures 3(a) and 3(b) represent the DOS for $TiSi_2$ allotropes; the Fermi level at 0 eV is marked with a vertical dashed line. The SCAN functional DOS calculation for C54 in Fig. 3(b) agrees with previous works using muffin-tin, Local Density Approximation (LDA), and Generalized Gradient Approximation functionals (GGA).[58,60,61]

A transition metal, such as Ti, has a d-orbital valence shell, and the d–d bond is a significant contributor to the cohesive energy of the lattices.[62,63] When an atom with an s and p shell, such as Si or Ge, is introduced into the transition metal lattice, the d–d bond lengthens reducing the bonds' contribution to lattice stability. In the case of silicide or germanide phases, a covalent hybridization between the transition metal d-orbital and the metalloid sp-orbital valence bands increases lattice stability. For this hybridization to take

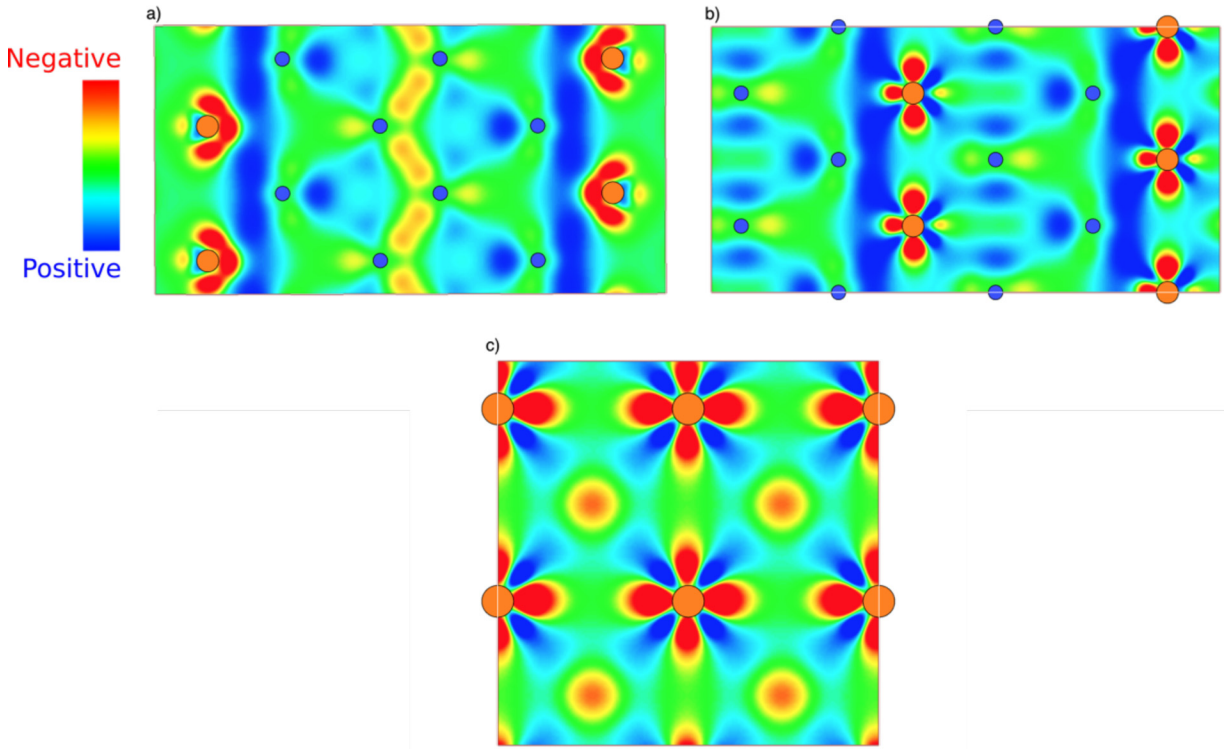

FIG. 4. Charge density difference plot of C49 $TiSi_2$ looking into the (100) (a), (001) (b), and (010) (c) planes. Si (blue) and Ti (orange) atoms are located within the cross section. The color legend represents the charge accumulation (red) and depletion (blue).

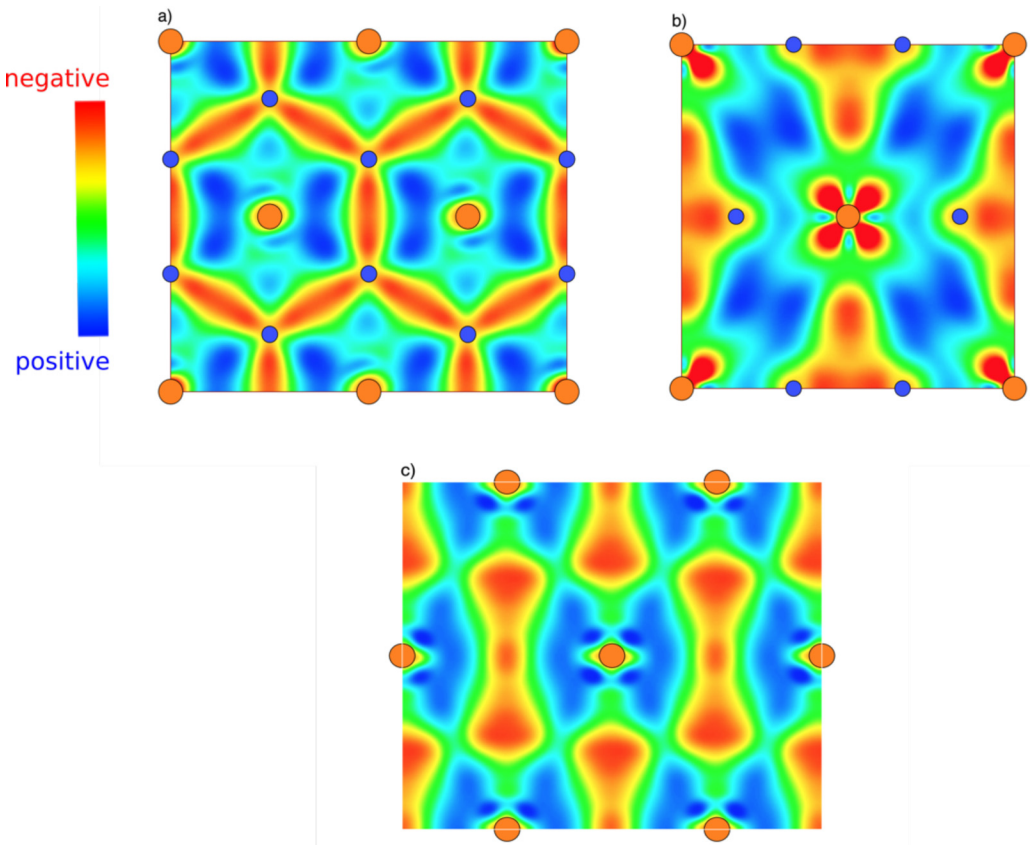

FIG. 5. Charge density difference plots for the C54 $TiSi_2$ looking into the (001) (a), (100) (b), and (010) (c) planes. Si (blue) and Ti (orange) atoms are located within the cross section. The color legend represents the charge accumulation (red) and depletion (blue).

place, the energy levels of the orbitals must overlap, and the crystal structure must have the correct symmetry to enable the hybridization. In the case of C54 $TiSi_2$, the symmetry of the allotropes forbids d states.[60] The interaction between Ti and Si atoms forms a bonding hybrid of the Ti d-orbitals and the p-orbitals, which causes an increase of stability. The hybrid bonding forms bonding orbitals below the Fermi level while antibonding and nonbonding orbitals form above the Fermi level. This behavior is observed with a total density of states plot as wide peaks above and below the Fermi level.

Although there is no bandgap, there is a region about the Fermi level which shows reduced electron density; this region has been called a pseudogap, and it arises from the bonding and antibonding associated with hybridization between atoms in the alloy.[64,65] There are two important features to the pseudogap. First, the location of the Fermi level relative to the pseudogap provides insight into stability; second, the depth of the pseudogap well at the Fermi level is related to the strength of the covalent bonding.[64–68]

A Fermi level lower in energy than the pseudogap indicates unfilled bonding orbitals.[66,67,69] Previous works have noted the relative stability of $TiSi_2$ C49 and C54 structures can be understood based on the position of the Fermi level.[60,61,68,70] However, previous works have not plotted the DOS to determine relative stability between the $TiGe_2$ C49 and C54 structures or the covalent stabilities between the $TiSi_2$ and $TiGe_2$ phases.

At the Fermi level, $TiSi_2$ C49 has a DOS of 0.18 states per eV for C49, while C54 has 0.4 states per eV, indicating more electrons are localized in covalent bonds in the C49 structure. Also, the Fermi level for the C49 structure in Fig. 3(a) is located at the minimum of the pseudogap, while the Fermi level for the C54 structure in Fig. 3(b) is slightly below it. Therefore, based on the Fermi level position, the $TiSi_2$ C49 allotrope (filled orbitals) is expected to be more stable than the C54 structure (unfilled orbitals).[60,61,68,70] The other measurement for stability, the enthalpy of formation shown in Table I, corroborates this conclusion, since C49 (−525 meV/atom) is more negative than C54 (−518 meV/atom).

Figures 3(c) and 3(d) show the DOS for $TiGe_2$; this system shows a pseudogap as well. The Fermi level for C49 $TiGe_2$ is at the pseudogap minimum as it was for C49 $TiSi_2$. However, in contrast to $TiSi_2$ C54, the Fermi level for C54 $TiGe_2$ is now at the pseudogap minimum, so the C54 $TiGe_2$ structure shows increased stability relative to $TiSi_2$. Therefore, unlike $TiSi_2$, C54 $TiGe_2$ has fully occupied bond orbitals. Also, the DOS at the Fermi level for C49 $TiSi_2$

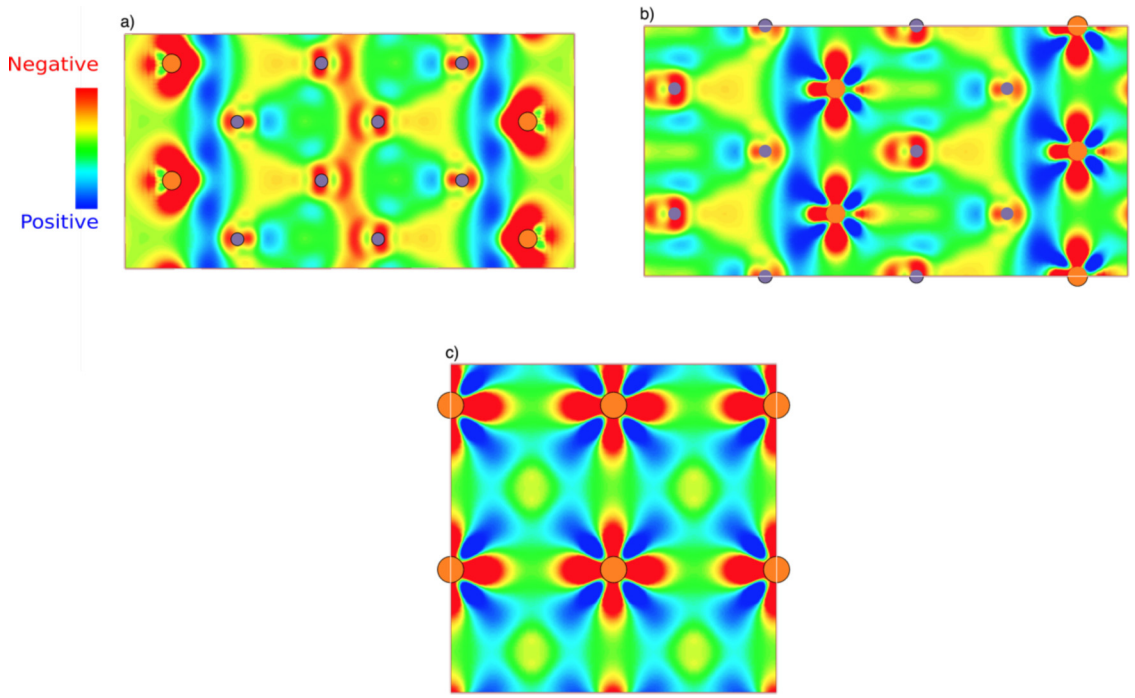

FIG. 6. Charge density difference plots for C49 $TiGe_2$ looking into the (001) (a), (100) (b), and (010) (c) planes. Ge (purple) and Ti (orange) atoms are located within the cross section. The color legend represents the charge accumulation (red) and depletion (blue). The system shows similar electron density to C49 $TiSi_2$ but more charge accumulation around the Ge atoms.

is 0.35 states per eV, while for C54 it is 0.31 states per eV. Based on the DOS in the pseudogap, it seems that the Ge interaction with Ti introduces additional hybridization thus stabilizing the structure. The DOS also suggests that the covalent bonding in C54 is stronger than in C49 $TiGe_2$. Again, this result from the $TiGe_2$ DOS is corroborated with enthalpy of formation in Table I. The stronger covalent bonding of C54 (−460 meV/atom) coincides with a more negative enthalpy of formation than C49 (−452 meV/atom).

The importance of an element's electronegativity for predicting alloy formation was first recognized by Miedema *et al.*[71] There is little difference in the Pauling's electronegativity of the elements: Ti (1.54), and Si (1.90) and Ge (2.01). The contribution of ionic bonding of a binary system, F_I, as opposed to covalent bonding, is often estimated as $F_i = 1 - \exp(-0.25\Delta X^2)$, where ΔX is the difference in the electronegativity of the components. This yields $F_i(TiSi_2) = 3.1\%$ and $F_i(TiGe_2) = 5.4\%$; this is, bonding for both systems is expected to be very largely covalent.

Interestingly, even though the electronegativity of Ni (1.91) is almost identical to that of Si. The ionic charges in fluorite-structured $NiSi_2$ were found to be +1.12 and −0.56.[72] That is, $NiSi_2$ shows a strong degree of ionicity, much larger than would be predicted by the simple analysis above. Therefore, to explicitly determine the degree of covalency, we perform Bader analysis to determine the charge transfer in the silicide and germanide systems. The charge transfer calculated from Bader analysis is given in Table VI. The C54 $TiSi_2$ phase shows significant ionicity, with the Ti atoms having charge +1.14e and Si atoms having charge −0.57e; interestingly, these are very similar to the values in $NiSi_2$, even though the structures are very different. The C49 structure shows slightly lower ionicity: the Ti has a charge of +1.10e, while the 2-NN and 4-NN Si atoms have charges of −0.61e and −0.43e, respectively. The lower charge at the 4-NN site is presumably due to the covalent bonding with two additional neighbors.

The charges in C54 $TiGe_2$ are identical to those in $TiSi_2$ despite the greater difference in the electronegativities. The C49 $TiGe_2$ structure also shows a very similar Ti charge to that in $TiSi_2$, but the apportionment of that charge to the 2-NN and 4-NN Si atoms is slightly different.

The charge transfer for C54 $TiSi_2$ was previously calculated by Wang *et al.*[58] They found the charge on Si to be −0.048e, which is less than 10% of the value determined here. Although this difference is large, variations of up to a factor of five in calculated ionic charge have been seen for different methods.[51] In particular, this difference can be explained in terms of the choice of functionals and charge analysis type. Wang *et al.* determined the Mulliken charges using GGA functional. Mulliken charge analysis has been described as potentially unphysical due to the strong dependence of the charges obtained on the basis set.[73–75] The Bader charge analysis has the advantage of independence of basis set and convergence to a stable value. Moreover, the more accurate SCAN functional[37] was not available at that time. Therefore, we believe that the values determined here are more likely to be accurate.

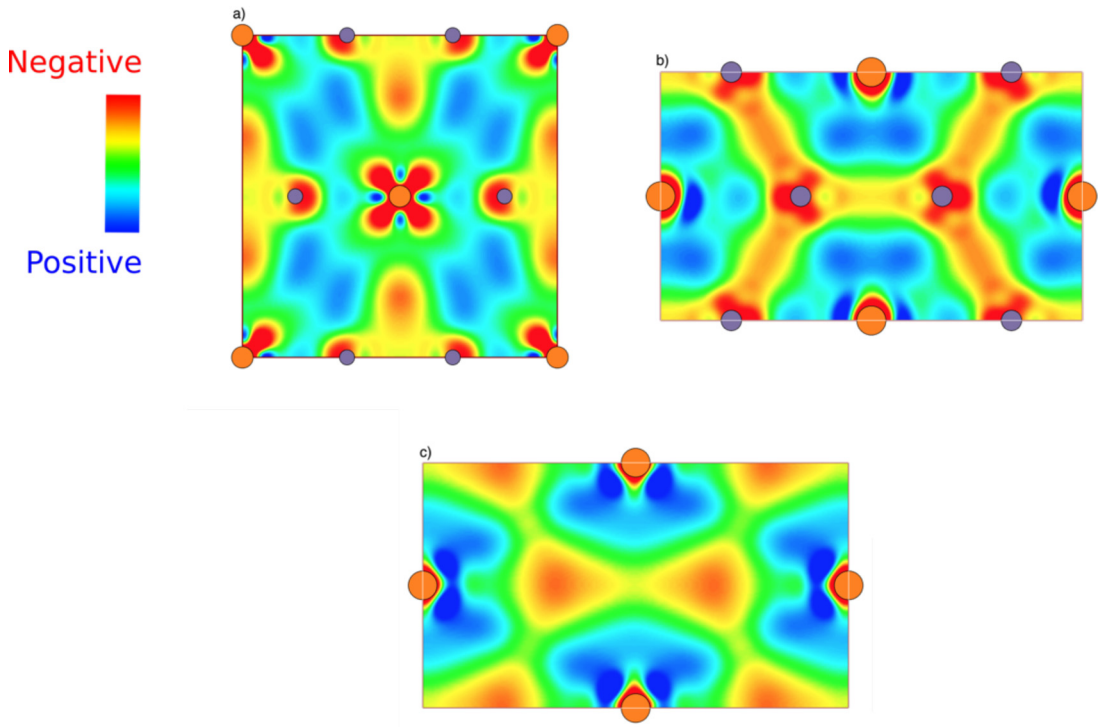

FIG. 7 Charge density difference plots for C54 $TiGe_2$ looking into the (001) (a), (100) (b), and (010) (c) planes. Ge (purple) and Ti (orange) atoms are located within the cross section. The color legend represents the charge accumulation (red) and depletion (blue). The system shows similar electron density to C49 $TiSi_2$ but more charge accumulation around the Ge atoms.

The charge density difference, CDD, is defined as the difference between the total charge density of the compound and constituent atoms, as discussed above. It, therefore, represents the charge redistribution when atoms are condensed to form a crystal. Thus, CDD is a valuable tool for assessing the degree of covalency and ionicity in a bond. Like Bader analysis, CDD is a method based on charge density from DFT; so, the visualizations it generates complement the charge transfer calculations in Table VI.

Figures 4–7 show the CDD plots for each system; the red regions represent charge accumulation, and the blue regions represent charge depletion. For the C49 allotrope, Figs. 4(a) and 4(b) show a depletion region between the stacks; this forms the boundaries of the layered structure illustrated in Fig. 1(c). The Ti atoms in Fig. 4(a) show little directionality of the charge accumulation, which indicates an absence of covalent bonding. These observations suggest that the layers are ionically bonded to each other, and that charge depletion region contributes to the high sheet resistance measured for C49 films observed from experiments.[1–4]

Figure 4(a) shows strong directional bonding between Si (blue) atoms through the center of the figure, which represents 3s–3p hybridization. Figure 4(c) shows directional bonding between Ti (orange) atoms; the bonding is denoted by the red region with a definite ellipsoid shape, which represents 3d–3d hybridization. Again, 3d–3d hybridization is observed between Ti atoms in Fig. 4(b). The regions between Ti and Si show charge depletion, so Fig. 4 suggests that there is no 3p–3d hybridization between the Si and Ti atoms. Bader analysis shows that the bonding between Ti and Si is due to partial charge transfer. We conclude that the observed CDD corroborates with the Bader charge analysis in Table VI.

In Fig. 4(b), a blue depletion region is observed between the Ti and Si atoms with an anisotropic charge density for Ti. The reduced charge on the Ti atom represents the charge transfer to Si. Figure 4(a) clearly shows more transfer of charge from the Ti to the 2-NN Si atoms than to the 4-NN Si atoms. This finding is not surprising due to the difference in the number of covalent bonds. Additionally, it is consistent with Bader analysis, which suggests that 2-NN Si atoms are more charged than the 4-NN Si atoms.

For C54, charge accumulation is shown between Si atoms in Fig. 5(a); three 3s–3p hybridization bonds link to three nearest neighbors. Figure 5(b) shows 3d–3d hybridization between the Ti atoms, with the charge accumulation being isotropic for the center Ti atom. Figures 5(a) and 5(c) show the charge depletion region around the Ti atoms, which relates to the charge transfer. The charge accumulation and depletion of the Ti atoms suggests an evenly

distributed charge transfer to the Si atoms; this is consistent with Bader charge analysis in Table VI. No charge accumulation is observed between Ti and Si because the symmetry of the C54 structure does not allow Ti d-orbital hybridization with the Si p-orbitals.[60,65] Figures 5(b) and 5(c) show charge accumulation at the interstitial sites of C54. The differences between the $TiSi_2$ C54 and C49 structures are the isotropic charge transfer and the covalent bonds. C54 does not have the layer of 4-NN Si atoms, which suggests less hybridization. So, the reduction of hybridized bonding explains the increase of formation energy, and the reduction of covalent stability from the DOS plots.

From Bader analysis, the $TiGe_2$ and $TiSi_2$ allotropes show similar charge transfer; the Ti atom in the $TiGe_2$ and $TiSi_2$ C54 allotrope both transfer 1.14e, while the Ti atom in the C49 structure transfer 1.08e and 1.10e, respectively. This similarity is also evident in the CDD in Figs. 6 and 7. Charge accumulation is noticeable between the Ti atoms in $TiSi_2$ in Figs. 4(b) and 4(c), indicating that 4d–4d hybridization also occurs for the C49 $TiGe_2$ system. In Fig. 6(a), the same directional charge transfer is observed between the Ge atoms, which relate to 4s–4p hybridization. However, the accumulation region is broader than in C49 $TiSi_2$, indicating that the hybridized orbitals are less bound than in $TiSi_2$. The introduction of the Ge atom increases the volume of the lattice structure which causes the d-orbital broadening. This broadening reduces the stability of the crystal; however, hybridization between a transition metal and metalloid makes the energy of the crystal more negative.[64,65] Figures 6(a) and 6(b) show charge accumulation between the Ge and Ti atoms indicating interaction; these panels suggest a 4s–4p hybridization between the unlike atoms.

Figure 7 illustrates the CDD for the $TiGe_2$ C54 allotrope, with charge transfer between the Ti and Ge, and the 3d–3d hybridization between Ti atoms. The accumulation region between Ge atoms is wider than between Si atoms in Fig. 5(a), indicating that the electrons are less bound between Ge atoms. Like $TiGe_2$ C49, these findings point to hybridization between the Ti and Ge and are consistent with the stability inferred from the DOS. Unlike $TiSi_2$ C54, the 4s–4p hybridization lowers the formation energy for $TiGe_2$ C54. The reason for this is the interaction between Ti and Ge introduces more hybridization of orbitals than is present in $TiSi_2$ C54. The CDD plot for $TiGe_2$ C54 shows charge accumulation between the atoms supporting the increased interaction relative to $TiSi_2$ C54. Overall, the $TiGe_2$ bonding has more bonding similarities to the $NiSi_2$ than to $TiSi_2$.[72,76]

DISCUSSION AND CONCLUSIONS

The enthalpy of formation calculations done here for the $TiSi_2$ phase is largely consistent with previous experimental and computational reports.[4,38,53,77] While previous experiments agree on the order of the formation, C49 and then C54, the reasons for this order are debated. This work has shown that the formation energy of C49 is lower than C54 and provides some physical arguments for why this is so. The vibrational free energy is added to calculate the temperature dependent Helmholtz free energy, but these calculations show the vibrational free energy does not drive the transformation of C54 to one of the other structures at higher temperatures.

Via *et al.*[78] performed 460 °C–540 °C anneals on $TiSi_2$ C49 to introduce defects followed by an anneal to form C54. Because the activation energy for the transformation increased with defect concentration; they concluded that this dependence is the reason for the inconsistent results on transformation kinetics among previous experiments. Defect energies were calculated using chemical potentials corresponding to various growth conditions; this work is consistent with the C49 allotrope as being much more prone to forming defects than the C54 allotrope, consistent with the experiments.[77,79] Therefore, this work suggests a component of the transformation competition is due to the low defect formation energies for $TiSi_2$ C49. Also, the data suggest growth in a Ti-rich environment will produce a $TiSi_2$ C49 allotrope with more defects; thus, the C49–C54 energy barrier may be lowered with higher Ti-rich concentrations. Moreover, the defect formation energy is expected to be between those of the pure $TiSi_2$ and $TiGe_2$ binary phases, so C49 $Ti(Si_{1-x}Ge_x)_2$ should have a low defect formation energy and a higher concentration of defects. Extending the knowledge of defect concentration and activation energy, the C49–C54 $Ti(Si_{1-x}Ge_x)_2$ transformation is expected to express the same trend.

As mentioned above, the $TiGe_2$ system does not show a C49 precursor phase for the formation of C54.[19,24] However, based on the work by Sun *et al.*,[55] this calculation for the $TiGe_2$ C49 energy is well below the upper limit for metastability. For the first time, this work shows the allotrope as potentially metastable; such metastability is consistent with the experiment.[25] When considering the Helmholtz free energy, the plot suggests the most stable phase is the C49 allotrope. Thus, the vibrational free energy does not drive the C54 free energy below C49. This result suggests the C54 is the most stable phase due to the spontaneous defect formation of $TiGe_2$ C49.

The $TiGe_2$ C40 phase is not observed during the solid reaction, but this work combined with that of Sun *et al.* supports the possibility of the metastability of the structure. Experiments have shown the existence of the $TiSi_2$ C40 structure using nanosecond laser annealing experiments, in which the rapid cooling rate quenches metastable phases.[17,26–28,80] Therefore, it seems possible that $TiGe_2$ C40 might be observable using the same nanosecond laser annealing techniques.

$Si_{1-x}Ge_x$ layers have become instrumental for introducing compressive strain to CMOS channels. The Ti-$Si_{1-x}Ge_x$ bilayer reaction forms the C54 structure of interest, but the $Ti(Si_{1-x}Ge_x)_2$ C54 structure forms at lower temperatures than $TiSi_2$ C54, which provides an improved thermal budget for semiconductor processing.[20] This work has developed a fundamental understanding of $TiGe_2$ C49 and C54 phases, which is useful for applying to the $Ti(Si_{1-x}Ge_x)_2$ system. The C54 structure is the $TiGe_2$ ground state structure because the Ge atom produces stable bonding orbitals. The extended Born model shows the stability of a binary alloy is a combination of ionic and covalent bonding. Based on these results, this work corroborates that the Ge atom lowers the formation energy of the $Ti(Si_{1-x}Ge_x)_2$ C54 phase with increasing Ge fraction.

ACKNOWLEDGMENTS

D.L.B. would like to acknowledge the Florida Education Fund's McKnight Doctoral Fellowship for funding this work and

HiperGator for providing the high-performance computer, which produced this work. He would also like to thank Michele Fullarton and Joshua Paul for useful discussions. We thank Ximeng Wang for computational support during the revision.

DATA AVAILABILITY

The data that supports the findings of this study are available within the article.

REFERENCES

[1]S. P. Murarka, D. B. Fraser, A. K. Sinha, and H. J. Levinstein, IEEE J. Solid-State Circuits **15**, 474 (1980).
[2]G. Ottaviani and C. Nobili, Thin Solid Films **163**, 111 (1988).
[3]F. M. d'Heurle, S. L. Zhang, C. Lavoie, P. Gas, C. Cabral Jr., and J. M. E. Harper, J. Appl. Phys. **90**, 6409 (2001).
[4]R. Beyers and R. Sinclair, J. Appl. Phys. **57**, 5240 (1985).
[5]D. B. Aldrich, H. L. Heck, Y. L. Chen, D. E. Sayers, and R. J. Nemanich, J. Appl. Phys. **78**, 4958 (1995).
[6]U. Gösele and K. N. Tu, J. Appl. Phys. **53**, 3252 (1982).
[7]F. M. d'Heurle and P. Gas, J. Mater. Res. **1**, 205 (2011).
[8]F. M. d'Heurle and R. Ghez, Thin Solid Films **215**, 19 (1992).
[9]S. Motakef, J. M. E. Harper, F. M. d'Heurle, T. A. Gallo, and N. Herbots, J. Appl. Phys. **70**, 2660 (1991).
[10]A. Mouroux, S. L. Zhang, W. Kaplan, S. Nygren, M. Östling, and C. S. Petersson, Appl. Phys. Lett. **69**, 975 (1996).
[11]H. K. Park, J. Sachitano, M. McPherson, T. Yamaguchi, and G. Lehman, J. Vac. Sci. Technol. A **2**, 264 (1984).
[12]J. Åberg, S. Persson, P. E. Hellberg, S. L. Zhang, U. Smith, F. Ericson, M. Engström, and W. Kaplan, J. Appl. Phys. **90**, 2380 (2001).
[13]R. V. Nagabushnam, R. K. Singh, and S. Sharan, Mater. Sci. Semicond. Process. **1**, 249 (1998).
[14]Y. M. Thu, K. M. Latt, and A. A. Bin Mohamed, AIP Conf. Proc. **1202**, 84–87 (2010).
[15]H. Jeon, C. A. Sukow, J. W. Honeycutt, G. A. Rozgonyi, and R. J. Nemanich, J. Appl. Phys. **71**, 4269 (1992).
[16]D. B. Aldrich, Y. L. Chen, D. E. Sayers, R. J. Nemanich, S. P. Ashburn, and M. C. Öztürk, J. Appl. Phys. **77**, 5107 (1995).
[17]S. C. Tan, L. Liu, Y. P. Zeng, A. See, and Z. X. Shen, J. Electrochem. Soc. **152**, G754 (2005).
[18]W. Freiman, A. Eyal, Y. L. Khait, R. Beserman, and K. Dettmer, Appl. Phys. Lett. **69**, 3821 (1996).
[19]J. B. Lai and L. J. Chen, J. Appl. Phys. **86**, 1340 (1999).
[20]H. Yu, M. Schaekers, J. Zhang, L.-L. Wang, J.-L. Everaert, N. Horiguchi, Y.-L. Jiang, D. Mocuta, N. Collaert, and K. De Meyer, IEEE Trans. Electron Devices **64**, 500 (2017).
[21]H. Yu, M. Schaekers, A. Peter, G. Pourtois, E. Rosseel, J.-G. Lee, W.-B. Song, K. M. Shin, J.-L. Everaert, S. A. Chew, S. Demuynck, D. Kim, K. Barla, A. Mocuta, N. Horiguchi, A. V.-Y. Thean, N. Collaert, and K. De Meyer, IEEE Trans. Electron Devices **63**, 4632 (2016).
[22]Y. Sun, S. E. Thompson, and T. Nishida, *Strain Effect in Semiconductors* (Springer US, Boston, MA, 2010).
[23]H. Yu, M. Schaekers, A. Hikavyy, E. Rosseel, A. Peter, K. Hollar, F. A. Khaja, W. Aderhold, L. Date, A. J. Mayur, J. G. Lee, K. M. Shin, B. Douhard, S. A. Chew, S. Demuynck, S. Kubicek, D. Kim, A. Mocuta, K. Barla, N. Horiguchi, N. Collaert, A. V. Y. Thean, and K. De Meyer, in *2016 IEEE Symposium on VLSI Technology* (IEEE, 2016), pp. 1–2.
[24]O. Thomas, S. Delage, F. M. d'Heurle, and G. Scilla, Appl. Phys. Lett. **54**, 228 (1989).
[25]Q. Z. Hong, K. Barmak, and F. M. d'Heurle, Appl. Phys. Lett. **62**, 3435 (1993).
[26]K. Li, S. Y. Chen, and Z. X. Shen, Appl. Phys. Lett. **78**, 3989 (2001).
[27]T. Yu, S. C. Tan, Z. X. Shen, L. W. Chen, J. Y. Lin, and A. K. See, Appl. Phys. Lett. **80**, 2266 (2002).
[28]S. Y. Chen, Z. X. Shen, K. Li, A. K. See, and L. H. Chan, Appl. Phys. Lett. **77**, 4395 (2000).
[29]G. Kresse and J. Hafner, Phys. Rev. B **47**, 558–561 (1993).
[30]P. Hohenberg and W. Kohn, Phys. Rev. **136**, B864 (1964).
[31]G. Kresse and J. Furthmüller, Comput. Mater. Sci. **6**, 15 (1996).
[32]G. Kresse and D. Joubert, Phys. Rev. B **59**, 1758 (1999).
[33]G. Kresse and J. Hafner, J. Phys.: Condens. Matter **6**, 8245 (1999).
[34]J. P. Perdew, K. Burke, and M. Ernzerhof, Phys. Rev. Lett. **77**, 3865 (1996).
[35]J. P. Perdew and A. Zunger, Phys. Rev. B **23**, 5048–5079 (1981).
[36]J. Sun, A. Ruzsinszky, and J. P. Perdew, Phys. Rev. Lett. **115**, 036402 (2015).
[37]M. Modrzejewski, G. Chalasinski, and M. M. Szczesniak, J. Phys. Chem. C **123**(13), 8047–8056 (2019).
[38]A. Jain, G. Hautier, C. J. Moore, S. Ping Ong, C. C. Fischer, T. Mueller, K. A. Persson, and G. Ceder, Comput. Mater. Sci. **50**, 2295 (2011).
[39]P. Wisesa, K. A. McGill, and T. Mueller, Phys. Rev. B **93**, 155109 (2016).
[40]H. T. Stokes and D. M. Hatch, J. Appl. Crystallogr. **38**, 237 (2005).
[41]P. E. Blöchl, O. Jepsen, and O. K. Andersen, Phys. Rev. B **49**, 16223 (1994).
[42]M. Methfessel and A. T. Paxton, Phys. Rev. B **40**, 3616 (1989).
[43]C. G. Van de Walle and J. Neugebauer, J. Appl. Phys. **95**, 3851 (2004).
[44]S.-H. Wei, Comput. Mater. Sci. **30**, 337 (2004).
[45]S. N. Sun, N. Kioussis, S.-P. Lim, A. Gonis, and W. H. Gourdin, Phys. Rev. B **52**, 14421 (1995).
[46]P. A. Korzhavyi, L. V. Pourovskii, H. W. Hugosson, A. V. Ruban, and B. Johansson, Phys. Rev. Lett. **88**, 015505 (2001).
[47]E. Sanville, S. D. Kenny, R. Smith, and G. Henkelman, J. Comput. Chem. **28**, 899 (2007).
[48]M. Yu and D. R. Trinkle, J. Chem. Phys. **134**, 064111 (2011).
[49]G. Henkelman, A. Arnaldsson, and H. Jónsson, Comput. Mater. Sci. **36**, 354 (2006).
[50]W. Tang, E. Sanville, and G. Henkelman, J. Phys.: Condens. Matter **21**, 084204 (2009).
[51]J. Liu, E. Tennessen, J. Miao, Y. Huang, J. M. Rondinelli, and H. Heinz, J. Phys. Chem. C **122**, 14996 (2018).
[52]H. Heinz and U. W. Suter, J. Phys. Chem. B **108**, 18341 (2004).
[53]C. Colinet, W. Wolf, R. Podloucky, and A. Pasturel, Appl. Phys. Lett. **87**, 041910 (2005).
[54]A. Jain, G. Hautier, S. P. Ong, C. J. Moore, C. C. Fischer, K. A. Persson, and G. Ceder, Phys. Rev. B **84**, 045115 (2011).
[55]W. Sun, S. T. Dacek, S. P. Ong, G. Hautier, A. Jain, W. D. Richards, A. C. Gamst, K. A. Persson, and G. Ceder, Sci. Adv. **2**, e1600225 (2016).
[56]A. Togo and I. Tanaka, Scr. Mater. **108**, 1 (2015).
[57]J. Nyman, O. S. Pundyke, and G. M. Day, Phys. Chem. Chem. Phys. **18**, 15828 (2016).
[58]T. Wang, Y. B. Dai, S. K. Ouyang, H. S. Shen, Q. K. Wang, and J. S. Wu, Mater. Lett. **59**, 885 (2005).
[59]L. Miglio, M. Iannuzzi, P. Raiteri, and M. Celino, Microelectron. Eng. **55**, 83 (2001).
[60]M. Ekman and V. Ozoliņš, Phys. Rev. B **57**, 4419 (1998).
[61]P. Ravindran, L. Fast, P. A. Korzhavyi, B. Johansson, J. Wills, and O. Eriksson, J. Appl. Phys. **84**, 4891 (1998).
[62]G. Frenking and N. Fröhlich, Chem. Rev. **100**, 717 (2000).
[63]H. Ehrenreich, Science **168**, 237 (1970).
[64]A. Pasturel, C. Colinet, and P. Hicter, Physica B + C **132**, 177 (1985).
[65]C. D. Gelatt, A. R. Williams, and V. L. Moruzzi, Phys. Rev. B **27**, 2005 (1983).
[66]A. J. Freeman, T. Hong, W. Lin, and J.-H. Xu, MRS Proc. **213**, 14 (2011).
[67]J.-H. Xu and A. J. Freeman, J. Mater. Res. **6**, 1188 (2011).
[68]C. Colinet, Intermetallics **11**, 1095 (2003).
[69]J. H. Xu, T. Oguchi, and A. J. Freeman, Phys. Rev. B **35**, 6940 (1987).
[70]P. Ravindran, G. Subramoniam, and R. Asokamani, Phys. Rev. B **53**, 1129 (1996).

[71]A. R. Miedema, F. R. de Boer, and P. F. de Chatel, J. Phys.: F Met. Phys. **3**, 1558 (1973).
[72]D. M. Bylander, L. Kleinman, K. Mednick, and W. R. Grise, Phys. Rev. B **26**, 6379 (1982).
[73]C. L. Fonseca Guerra, J.-W. Handgraaf, E. J. Baerends, and F. M. Bickelhaupt, J. Comput. Chem. **25**, 189 (2003).
[74]T. A. Manz and N. G. Limas, RSC Adv. **6**, 47771 (2016).
[75]N. G. Limas and T. A. Manz, RSC Adv. **6**, 45727 (2016).
[76]J. Tersoff and D. R. Hamann, Phys. Rev. B **28**, 1168 (1983).
[77]Z. Ma and L. H. Allen, Phys. Rev. B **49**, 13501 (1994).
[78]F. La Via, F. Mammoliti, and M. G. Grimaldi, Appl. Phys. Lett. **85**, 5577 (2004).
[79]T. C. Chou, C. Y. Wong, and K. N. Tu, J. Appl. Phys. **62**, 2275 (1987).
[80]F. L. Via, F. Mammoliti, and M. G. Grimaldi, J. Appl. Phys. **91**, 633 (2002).